図4　心筋症におけるトロポニンの遺伝子変異と筋カルシウム感受性
心筋症の遺伝子変異は TnT1, C-TnT に多く, 筋カルシウム感受性を修飾する.

ルシウムセンシタイザーは phoshodiesterase の阻害作用も併せてもっており, 細胞内 cyclic-AMP の増加によって筋小胞体からのカルシウムイオン放出が増加し, ついにはカルシウム overload となる可能性や[7], 構造が類似した他の蛋白と相互作用があるなど, 薬剤としての標的特異性が低いことが原因として考えられる. 拡張型心筋症例では, 少なくとも一部の症例でカルシウム感受性の低下と収縮不全の関連が示唆されている. これらの事実は TnC や TnT を特異的に制御する化合物の設計により, 新たな強心剤の開発の可能性を示している.

一方, 肥大型心筋症 (HCM) ではトロポニンの遺伝子変異によりカルシウム感受性が亢進することが発病に関連する可能性が示唆されている. 同患者の遺伝子解析によると, 約15％の患者に TnT の遺伝子変異が認められる. 大槻らによれば[5]トロポニンがアクチン/トロポミオシンと直接接触する部分 (TnT1, C-TnT, TnI

調節領域) に変異が多く認められ, コアドメインには変異は少ないという (図4). 変異 TnT の交換導入を行った心筋スキンドファイバーを用いた研究で, カルシウムイオン濃度–張力関係の左方シフト, すなわちカルシウム感受性の亢進が認められた. この結果から TnT の変異により, カルシウム感受性が亢進し, 収縮増加と弛緩不全という肥大型心筋症に特有の症状が発症するという有力な仮説が生まれる. TnT の変異によるカルシウム感受性亢進のメカニズムを原子構造で解明すると, 肥大型心筋症に特異的に作用する薬剤の設計を期待できる. 原因となる遺伝子変異ごとに構造が異なる薬剤設計が求められる可能性もある. 言い換えれば, 心筋トロポニンの変異に基づく肥大型心筋症の治療法の開発はテーラーメード医療のモデルケースとなる可能性がある.

細胞膜(リン脂質)

ホスホリパーゼ群

5-LO
FLAP

アラキドン酸 ------→ 種々の細胞 LT類
(ロイコトリエン)

シクロオキシゲナーゼ
(COX-1とCOX-2)

アスピリン
インドメタシン

PGH_2

合成酵素群

mPGES

血小板ほか　肥満細胞　種々の細胞　血管内皮　胎盤ほか
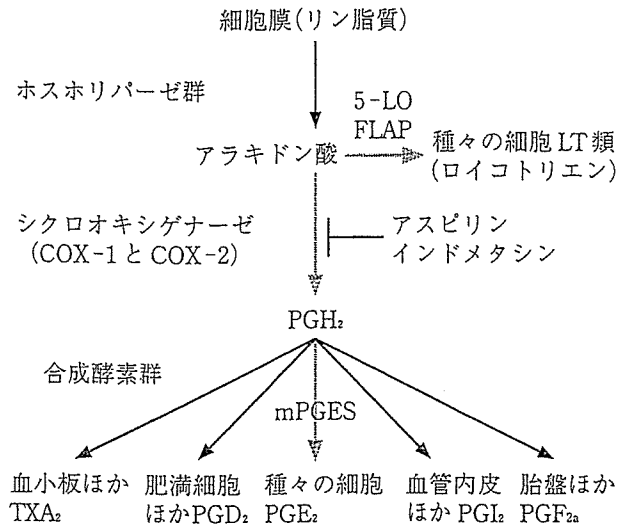TXA_2　ほかPGD_2　PGE_2　ほかPGI_2　$PGF_{2\alpha}$

図5　プロスタグランジン産生系

3. 創薬の標的として注目されている プロスタグランジン合成酵素群の 構造解析

シクロオキシゲナーゼ(COX)はプロスタグランジン(PG)を生合成する律速酵素として知られている(図5)2種類のアイソザイムが存在する. COX-1はconstitutive enzymeと呼ばれ, ほとんどの細胞で常時発現しており, 生体の安定性を維持する役割を果たす. 一方, COX-2はinducible enzymeとして, 単球, 線維芽細胞, 滑膜細胞などの炎症にかかわる細胞で発現し, 炎症性サイトカインなどによって誘導される. 従来の非ステロイド系抗炎症剤は, COX-1とCOX-2の両方を阻害するために炎症巣のPGだけでなく, 胃粘膜や腎でのPG(特にPGE_2)産生を抑制し胃や腎の副作用を合併する. そこで, 炎症に深く関与していると考えられるCOX-2だけを選択的に阻害する薬剤の開発が進められてきた. このようにして開発されたCOX-2阻害薬は胃潰瘍を起こしにくい鎮痛剤として好んで投薬されていた. しかしながら, 2004年末, 米政府は, これらのCOX-2選択的阻害薬の3剤を心筋梗塞や脳梗塞の危険性を高める恐れがあるとして, 心臓病患者への処方や多量の長期使用を避けるよう勧告した. COX-2の下流に位置するプロスタサイクリン合成酵素の作用も

抑制するために, 同酵素に由来する抗血栓性作用や血流増加作用が損なわれることが原因ではないかと考えられている[8]. 図5に示したようにCOX-2の下流には多くの合成酵素があってそれぞれの作用を有する蛋白を合成している. 個々の合成酵素を選択的に阻害する薬剤の開発が次世代の創薬の標的として注目される. PGE_2の産生にかかわるmPGESを阻害する薬物の開発は血管内血栓形成を伴わない理想的な抗炎症剤となる可能性がある. TXA_2産生を阻害する薬剤の開発は血管内血栓形成の予防, 局所血流増加作用を通じて脳梗塞, 心筋梗塞の予防薬や治療薬として期待できる. PGI_2は既に難病といわれた原発性肺高血圧症の治療に有効であることが知られている. PG関連薬剤の開発は構造に基づく創薬の最大の標的の一つになっており, ナノメディシンプロジェクトでも複数の関連酵素の構造解析に取り組んでいる.

4. ナノメディシンプロジェクトの そのほかの研究

本プロジェクトでは分子構造イメージングに関連して上記のほかに, 細胞内イオン環境や, 血管新生にかかわる蛋白など幾つかの蛋白構造についても研究を進めている(国立循環器病センター研究所). 国立精神神経センターではin-silicoスクリーニング法によるParkinson病の治療薬探索に蛋白構造情報を応用する研究を進めている. 国立医薬品食品衛生研究所では原子間力顕微鏡を用いて蛋白表面の詳細な構造を解析することなどを通じて, 医用材料作成に向けた応用研究に取り組んでいる.

一方, 分子機能イメージングの領域では, 国立循環器病センターの望月らが増殖因子(EGF)刺激に伴うRas分子の活性化をFRET法で可視化できることをNature誌に報告した[9]. ナノメディシンプロジェクト開始後も血管内皮の走化運動にかかわるRap1蛋白の可視化に関する研究などにFRET法による分子イメージングを展開している. 国立精神神経センターの研究グループでは分子機能イメージング技術を応用してシナプス機能, プリオン蛋白質の機能の評価に

取り組み Proc Natl Acad Sci などの雑誌に研究成果を報告している[10].

お わ り に

本ナノメディシンプロジェクトでは循環器治療の中核施設である国立循環器病センター内に構造生物学ラボを立ち上げ, 分子特異的な治療薬の開発を目指している. ナノ DDS 技術や分子機能イメージング技術に関する研究を併せて推進することで, 特異的分子治療薬の分子輸送技術開発と他の分子との相互作用の可視化技術を推進することが可能となる. これにより, 分子診断・分子治療・分子評価を包含するテーラーメード医療の基盤形成に貢献したい.

■文　献━━━━━━━━━━━━━━━━━━━━━━━━━━

1) Patick AK, et al: Activities of the human immunodeficiency virus type 1 (HIV-1) protease inhibitor nelfinavir mesylate in combination with reverse transcriptase and protease inhibitors against acute HIV-1 infection in vitro. Antimicrob Agents Chemother　41: 2159-2164, 1997.

2) Drucker BJ, et al: Effects of a selective inhibitor of the Abl tyrosine kinase on the growth of Bcr-Abl positive cells. Nat Med　2: 561-566, 1996.

3) Takeda S, et al: Structure of the core domain of human cardiac troponin in the Ca^{2+} saturated form. Nature　424: 35-41, 2003.

4) 前田雄一郎ほか: トロポニンの結晶構造とカルシウム調節のメカニズム. 蛋白質 核酸 酵素　48: 500-512, 2003.

5) 大槻磐男: 筋収縮カルシウム受容調節の分子機構と遺伝性機能障害. 日薬理誌　118: 147-158, 2001.

6) Lee JA, et al: Effects of pimobendan, a novel inotropic agent on intracellular calcium and tension in isolated ferret ventricular muscle. Clin Sci　76: 609-618, 1989.

7) Nieminen MS, et al: Executive summary of the guidelines on the diagnosis and treatment of acute heart failure: The task force on acute heart failure of the European society of cardiology. Eur Heart J　26: 384-416, 2005.

8) Mukherjee D, et al: Risk of cardiovascular events associated with selective cox-2 inhibitors. JAMA　286: 954-959, 2001.

9) Mochizuki N, et al: Spatio-temporal images of growth-factor-induced activation of Ras and Rap1. Nature　411: 1065-1068, 2001.

10) Itami C, et al: Brain-derived neurotrophic factor-dependent unmasking of silent synapses in developing mouse barrel cortex. Proc Natl Acad Sci USA　100: 13069-13074, 2003.

X-band Thermionic Cathode RF Gun and Multi-Beam Compton Scattering Monochromatic Tunable X-ray Source

Fumito SAKAMOTO,* Mitsuru UESAKA, Katsuhiro DOBASHI, Atsushi FUKASAWA and Tomohiko YAMAMOTO
Nuclear Professional School, The University of Tokyo 2-22 Shirakata-Shirane, Tokai, Naka, Ibaraki 319-1188, Japan

Junji URAKAWA, Toshiyasu HIGO and Mitsuo AKEMOTO
High Energy Accelerator Research Organization 1-1 Oho, Tsukuba, Ibaraki 305-0801, Japan

Kenichi MATSUO and Hisaharu SAKAE
Ishikawajima-Harima Heavy Industries Co., Ltd. 1 Shin-Nakahara, Isogo, Yokohama, Kanagawa 235-8501, Japan

Masashi YAMAMOTO
Akita National College of Technology 1-1 Iijima-Bunkyo, Akita, Akita 011-8511, Japan

A Compton scattering X-ray source consisting of an X-band (11.424 GHz) electron linear accelerator (linac) and Q-switched Nd:YAG laser is currently under construction. Monochromatic hard X-rays are required for a variety of medical and biological applications. The new hard X-ray source produces monochromatic X-rays via collision between a 35-MeV multi-bunch (10^4 bunches in a 1 μs RF pulse) electron beam and 1.4 J/10 ns (532 nm) Nd:YAG laser beam. The linac uses an X-band 3.5-cell thermionic cathode RF gun and an alpha magnet as an injector. The thermionic cathode RF gun is the first of its kind and can generate a high current (2 μA) and a multi-bunch 2-MeV electron beam. To increase the efficiency of the X-ray yield, a laser pulse circulation system is adopted, that can increase the X-ray intensity by up to 50 times. This scheme can produce monochromatic tunable X-rays (10 ~ 40 keV) with intensities of 10^8 ~ 10^9 photons/sec. In addition, the X-ray energy can be changed rapidly over 40 ms by two different wavelength lasers (YAG fundamental (1064 nm), 2nd harmonic (532 nm)) and an optical switch. This quick energy change is very important for living specimens and is very difficult to achieve in light sources such as a large SR (Synchrotron Radiation) source. The system can be used for dual-energy X-ray CT and subtraction X-ray CT to determine the 3D distribution of the atomic number density and electron density, and specified atomic distribution, respectively. In this paper, we describe the details of the system, report on experiments on the X-band thermionic cathode RF gun, and discuss applications of monochromatic X-rays.

PACS numbers: 29.27.Eg, 87.62.+n
Keywords: X-ray source, Compton scattering, X-band linac, X-band thermionic cathode RF gun

I. INTRODUCTION

X-rays of 10 ~ 40 keV are of great use in medical science, biology, and material science. Example techniques that use such X-rays are dynamic intravenous coronary arteriography (IVCAG) [1,2] and monochromatic X-ray imaging. In addition, the techniques of dual energy X-ray CT [3] and subtraction imaging using a contrast agent and dual energy X-rays may be realized by using two monochromatic X-ray beams.

Intense hard X-rays are generated by third-generation light sources. However, most synchrotron radiation (SR) sources are too large to be widely used for monochromatic X-rays. Therefore, we are developing a compact monochromatic X-ray (10 ~ 40 keV) source based on laser-electron collisions in an X-band (11.424 GHz) linear accelerator (linac) system [4-8] at the Nuclear Professional School, the University of Tokyo. Since the scattering angle of the photon depends on its energy, one to ten percent narrow-band X-rays are generated by collimating scattered photons.

In our system, a multi-bunch electron beam generated by a thermionic cathode RF gun is collimated and compressed temporally by an alpha magnet and

*E-mail: saka@nuclear.jp; uesaka@nuclear.jp;
Tel: +81-29-287-8413; Fax: +81-29-287-8488

Table 1. Performance of linac/laser Compton scattering X-ray sources.

| Laboratory	Electron energy	Charge	Wavelength and energy of laser pulse	X-ray energy and intensity	Fluctuation of X-ray
SHI [16]	14 MeV (S-band)	400 pC Single bunch	800 nm, 300 mJ, (Ti:Sapphire, 300 ps)	3.5 keV <10^4 photons/shot	50 %
MXI Systems Inc [15]	25 MeV (S-band)	500 pC Single bunch	1 μm, 20 J (Nd:Glass)	12 ~ 50 keV 10^8 photons/sec	50 %
LLNL [17]	57 MeV (S-band)	250 pC Single bunch	780 nm, 400 mJ (Ti:Sapphire, fs)	40 ~ 80 keV 10^7 photons/sec	50 %
SLAC [18]	60 MeV (X-band)	500 pC Single bunch	800 nm, 300 mJ (Ti:Sapphire, fs)	20 ~ 85 keV 10^8 photons/sec	80 %
U. Tokyo/NIRS/KEK [5]	35 MeV (X-band)	20 pC × 10000 Multi-bunch	1 μm, 2 J, (Nd:YAG, 10 nsec)	33 keV 10^8 photons/sec	<10 %
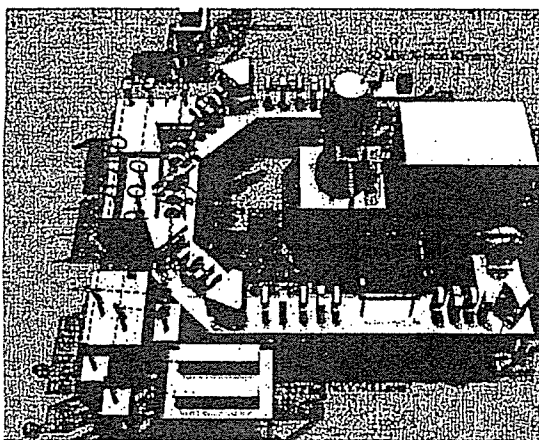
Fig. 1. Schematic of the compact X-ray source based on the X-band thermionic cathode RF-gun, and X-band accelerating structure and a Q-switched Nd:YAG laser.

accelerated by an X-band accelerating structure. The thermionic cathode RF gun can generate a high-current (2 μA) multi-bunch (10^4 bunches in 1 μs) electron beam. The experimentally confirmed energy of the electron beam generated by the RF gun is 2 MeV. The electron beam is bent by achromatic bends and focused at the collision point (CP). An approximately 10-ns hard X-ray is generated via Compton scattering upon laser-electron collision. This system can also generate dual energy monochromatic hard X-rays by using two Nd:YAG lasers. The laser system for Compton scattering is composed of a Q-switched Nd:YAG laser.

To demonstrate the proposed X-ray source, an X-band linac beam line (shown in Fig. 1) for a proof-of-principle experiment is under construction. The X-ray yield by the electron beam and a Q-switched Nd:YAG laser of 2.5 J/10 ns (1064 nm) is 10^7 photons/RF-pulse (10^8 photons/sec at 10 pps). A demonstration X-band beam line is being commissioned. We are also designing a laser cir-

culation system [9] to increase the X-ray yield up to 10^8 photons/pulse (10^9 photons/sec).

In this paper, we present the design and numerical analysis of the demonstration X-ray source system. The first experimental verification of the X-band thermionic cathode RF gun is also described.

II. BRIEF REVIEW OF LINAC-LASER COMPTON SCATTERING X-RAY SOURCE

Early experimental demonstrations of proof-of-principle systems have been made at LBL [10,11], BNL [12], KEK-JAERI-U.Tokyo [13] and at other installations in the 1990s. The use and distribution of table-top Ti:Sapphire lasers, CO_2 lasers, Nd:Glass lasers and RF photoinjectors have contributed to the development of the systems. In particular, developments have recently allowed the second harmonic to be produced as well as the fundamental [14]. The existing systems are specialized for medical and bio-scientific uses, such as for monochromatic X-ray imaging, dual-energy X-ray CT, subtraction X-ray CT, angiography, Auger cascade therapy, protein structural analysis, etc. These systems are summarized in Table 1. Of particular note is the pioneering work on medical monochromatic X-ray imaging performed by Carroll et al. [15]. Most system use scattering between a single electron bunch and a single laser pulse and hence cannot achieve X-ray intensities as high as 10^8 photons/sec [16–18]. Dynamic imaging, angiography and protein structural analysis are difficult without a high intensity. To address this problem, multiple scattering between multi-electron-bunches and multi-laser-pulses could be employed to generate an X-ray intensity of more than 10^9 photons/sec.

We define here the first and second generation of scattering in X-ray sources. The first generation established the following:
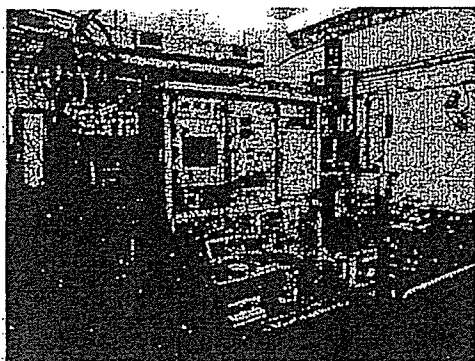
Fig. 2. Klystron and modulator (Toshiba E3768A).

Fig. 3. X-band thermionic cathode RF gun (Ishikawajima-Harima Heavy Industry Co., Ltd).

• First demonstration and application,
• Intensity up to 10^8 photons/sec,
• Intensity fluctuation due to time-jitter between electron beam and laser pulses.
The second generation will realize the following:
• Multi-scattering of electron beam and laser pulses,
• Intensity of more than 10^9 photons/sec,
• Variety of applications in medicine, protein structural analysis, nondestructive evaluation, and nuclear engineering.

In this paper, we report on the development a typical second-generation system underway at the University of Tokyo. We note that, KEK is developing a multibunch S-band photoinjector for the Global Linear Collider, which can produce more than 100 nC per RF pulse [19]. This system may be a second candidate for the second-generation source.

III. COMPTON SCATTERING X-RAY SOURCE BASED ON X-BAND LINAC

We detail here a compact X-ray source based on the proposed X-band linac shown in Fig. 1. A multi-bunch electron beam generated by a thermionic cathode RF gun is accelerated by an X-band accelerating structure. The beam is bent and focused at the collision point. Approximately 10 ns X-rays are generated via Compton scattering on laser-electron collision.

1. X-band Linac

An X-band linac is used with the compact hard X-ray source. The RF wavelength of the X-band is 1/4 of the S-band (2.856 GHz). However, the maximum field gradient of ~40 MV/m gives remarkable compactness.

A 0.7-m long X-band accelerating structure is used for the X-ray source. The X-band accelerating structure technology developed for future linear colliders [19] at
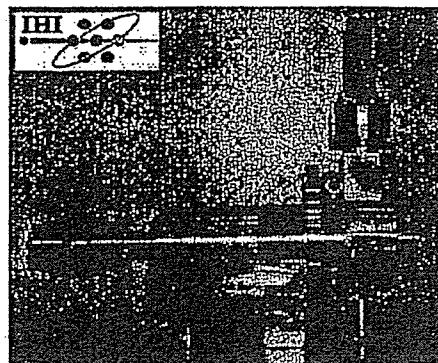
Table 2. Beam parameters at collision point.

Beam energy	35 MeV
Charge/bunch	20 pC
Bunches/RF pulse	10^4
Beam size (rms) (x,y)	100, 100 μm
Normalized emittance (rms) (x, y)	10, 10 πmm-mrad

KEK and Stanford Linear Accelerator Center (SLAC) are fully adopted for this system. Initially, the Round Detuned Structure (RDS) is to be adopted and is already being manufacturing.

We adopt a Periodic Permanent Magnet (PPM) type X-band klystron (Toshiba E3768A) designed for linear colliders [20]. The klystron modulator is being designed to fit the X-ray source. The nominal RF power is above 50 MW in 1 μs.

The beam optics of the X-band linac beam line were designed using SAD (Strategic Accelerator Design) [21] code. Photographs of the klystron/modulator are shown in Fig. 2. The beam parameters at the collision point (CP) are shown in Table 2.

2. 3.5-cell X-band Thermionic Cathode RF Gun

The injector of the system consists of an X-band thermionic cathode RF gun and an alpha magnet. The inner slit of the alpha magnet is used to eliminate low-energy particles. It is also used as a bunch compressor. Fig. 3 shows the X-band thermionic cathode RF gun. The detailed design and manufacture were performed by Ishikawajima-Harima Heavy Industries Co., Ltd. (IHI). The cavity of the RF gun has three full cells and a half cell (see Fig. 4) and is operated at 11.424 GHz in the π mode. The nominal beam energy is 2 MeV. A coaxial coupler [22] is introduced to ensure axial symmetry of the field in the gun and for placement inside a solenoid coil. The thermionic cathode is a dispenser type, and
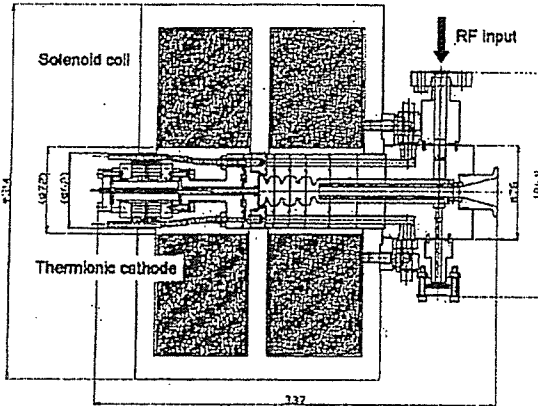
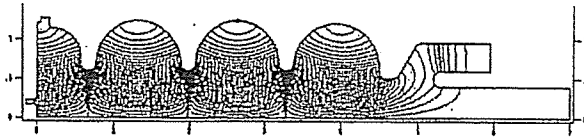Fig. 4. Cut-away view of the X-band thermionic cathode RF gun cavity.

Fig. 5. Electric field of the 3.5-cell X-band thermionic cathode RF gun. Red lines show the rH_ϕ contours.

the material is tungsten. The edge of the cathode is manufactured to reduce the radius size R to avoid concentration of the electric field at the edge. Tuning of the cavity can be controlled by moving the cathode position with a cathode plug. The thermionic cathode is operated at a current density of 20 A/cm^2, and its temperature is about 1000 °C. The radius of the effective emission area is 1.4 mm, hence, the output current is 1.23 A. Emission continues during the accelerating phase, that is 180°, and the emission rate is constant under a high voltage. The charge emitted in a RF period is given by

$$Q_{emit} = \frac{1}{2} \frac{\pi r_{cath}^2 \phi}{f_{RF}}, \qquad (1)$$

where r_{cath} is the radius of the effective emission area, ϕ is the flux of the cathode current, and f_{RF} is the RF frequency in the cavity. In our case, the charge per bunch is 53.9 pC. The other properties of the cavity were calculated by using SUPERFISH [23]. The contour lines rH_ϕ of the field in the cavity are shown in Fig. 5 and the properties of the cavity are listed in Table 3.

Since the energy spread after the main acceleration must be less than 1 %, beams from the injector must satisfy the following relation:

$$\delta = \frac{\Delta E_{inj} + E_{acc} \Delta \phi_{inj}^2}{E} < 0.01, \qquad (2)$$

where ΔE_{inj} is the energy spread at the injector, $\Delta \phi_{inj}$ is the bunch length in radians, and E_{acc} is the energy

Table 3. Properties of the 3.5-cell gun cavity, calculated by using SUPERFISH.

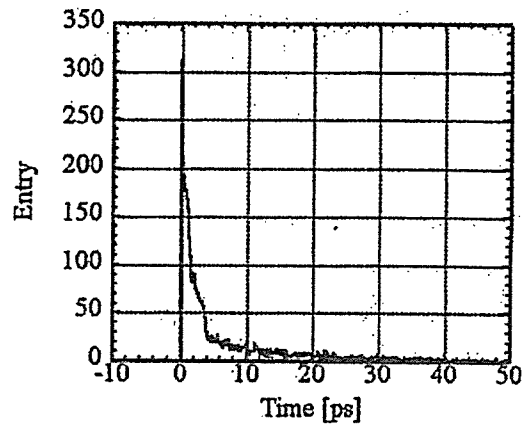|	
Resonant frequency	11.424 GHz
Transit time factor	0.703
Shunt impedance	2.46 MΩ
Q value	9350
Wake loss parameter	7.72 V/pC

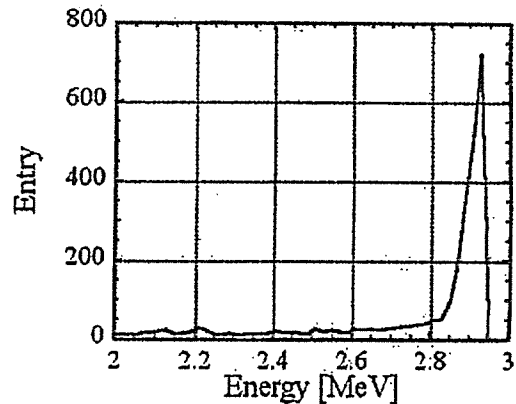Fig. 6. Bunch form before the alpha magnet (simulation).

Fig. 7. Energy spectrum before the alpha magnet (simulation).

gain in the main accelerating structure. The dynamics of the particles in the gun cavity were simulated by using PARMELA [24]. The total charge was found to be 41 pC. The bunch length was 4.4 ps, and the energy spread was 0.16 MeV (rms over 2.25-MeV particles) (Figs. 6 and 7). The field gradient on the cathode surface is about 140 MV/m. Since δ becomes 0.01, lower particles should be eliminated. As Fig. 8 shows, when particles of energy less than 2.8 MeV are cut-off, the bunch satisfies the energy spread condition.

Table 4. Bunch parameters after the alpha magnet (simulation results).

Position of slit	121 mm	122 mm
Charge	20.2 pC	7.5 pC
Energy	2.92 ± 0.02 MeV	2.94 ± 0.01 MeV
Cut-off energy	2.86	2.91
Normalized emittance	15.1, 6.3 πmm-mrad	10.2, 4.1 πmm-mrad
Bunch length	2.2 ps	1.0 ps
δ	0.024	0.005
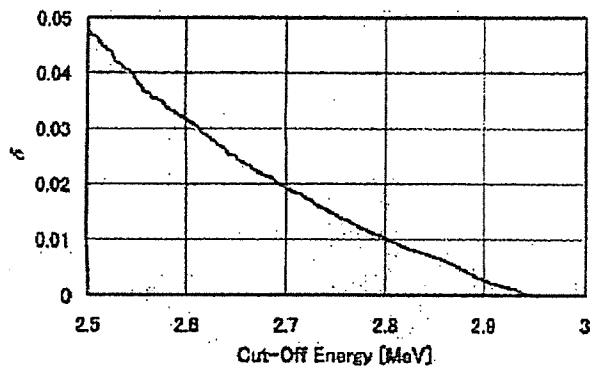
Fig. 8. Relation between the cut-off energy and the estimated energy spread after main acceleration (simulation).
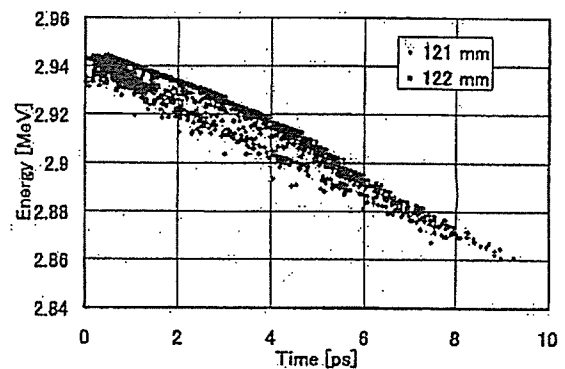

Fig. 9. Particle distribution in time-energy space. The blue dots are for a slit position of 121 mm, and the red dots are for 122 mm (simulation).

Next, the motion in the alpha magnet was calculated. The alpha magnet features a slit to cut out low-energy particles. By moving this slit, the cut-off energy can be controlled. Fig. 9 shows the particle distribution in time-energy space for different slit positions. The bunch parameters after the alpha magnet are listed in Table 4. When the slit position is 121 mm, the condition is not satisfied. It is satisfied for 122 mm, though the charge becomes small. The cut-off energy is higher than that previously estimated. This is because over bunching occurs in the alpha magnet, increasing the bunch length. To obtain the best compression and a high charge, the field gradient in the alpha magnet has to be higher. However, since it is difficult to increase the field, the energy should be decreased.

3. Laser System

Concentrating on the R&D of the accelerator, we chose a commercial and reliable laser for laser-electron collision. To realize a compact system, we used two Q-switched Nd:YAG lasers with an intensity of 2.5 J/pulse (1:4 J/pulse for the second harmonic), a repetition rate of 10 pps, a pulse duration of 10 ns (FWHM), and a wavelength of 1064 nm (fundamental).

In the second step, immediately switching the X-ray energy, we added a second laser system. The laser sys-
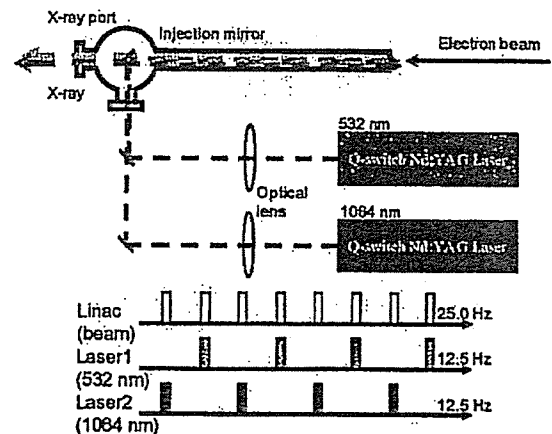

Fig. 10. Concept of the dual energy X-ray generation system.

tems for the fundamental and the second harmonics are fired in turn. In this way, we can generate dual energy monochromatic X-rays with a repetition rate of 12.5 Hz (if the repetition rate of the linac is 25 Hz), as shown in Fig. 10. The advantage of this dual energy X-ray generation system is that the switching of the X-ray energy with a high repetition rate is very useful for dynamic subtraction imaging and dual energy X-ray CT. To increase
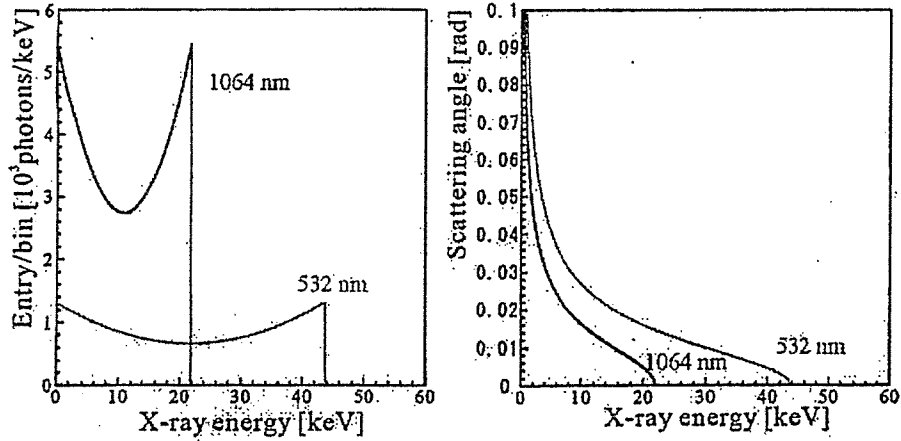
Fig. 11. Energy spectrum of X-rays for laser wavelengths of 1064 nm and 532 nm with an electron energy of 35 MeV.
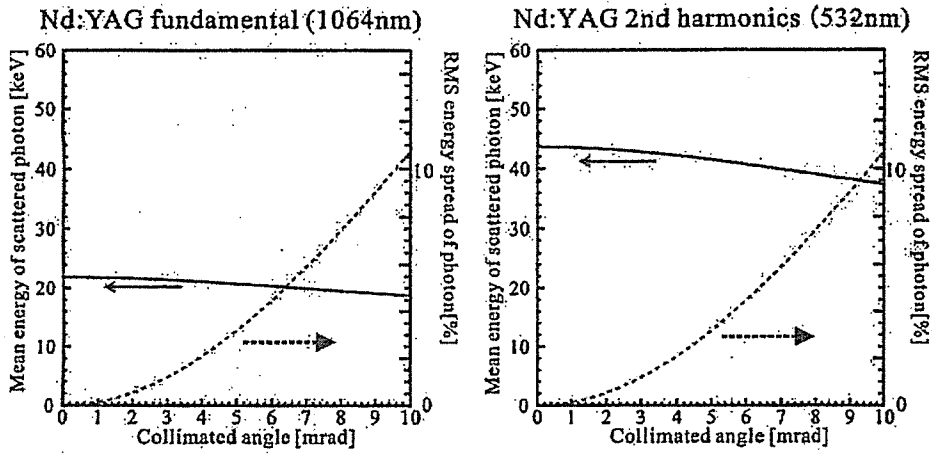

Fig. 12. Energy spread in the rms and the mean energies of available X-rays for each collimated angle.

Table 5. Properties of the X-rays generated with electron beam energy of 35 MeV and charge of 20 pC/bunch.

Laser wavelength	1064 nm	532 nm
Pulse energy of laser (J/pulse)	2.5	1.4
X-ray yield (photons/sec)	1.0×10^9	4.4×10^8
Cut-off energy (keV)	2.86	2.91
Maximum X-ray energy (keV)	21.9	43.8

energy distribution and the relationship between the energy and the scattering angle of the X-ray for each laser wavelength with electron beam energy of 35 MeV are shown in Fig. 11. The properties of the X-rays are summarized in Table 5. Fig. 12 shows the mean energy and the rms energy spread of the available X-rays for each laser wavelength as functions of the scattered photons collimation angle.

the X-ray yield, we need to design a technique for the circulation of the laser pulse to enhance the luminosity by 10 times.

4. X-ray Yield and Properties

The X-ray yield per bunch is calculated from the cross section of Compton scattering and the luminosity. The

IV. TEST OF THE X-BAND RF SOURCE AND THE X-BAND THERMIONIC CATHODE RF GUN

1. High-power Generation and RF Conditioning of the X-band RF Source

RF conditioning is required for the RF windows and circuit components, such as the RF waveguides. The ex-
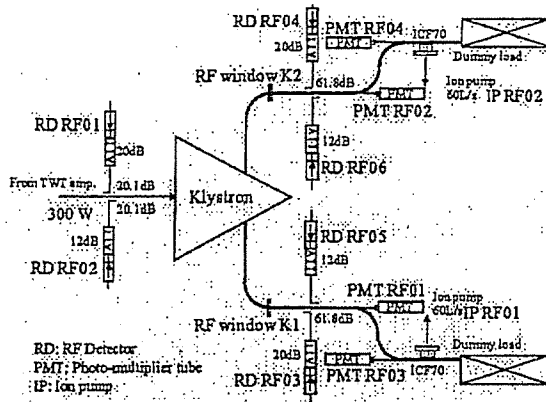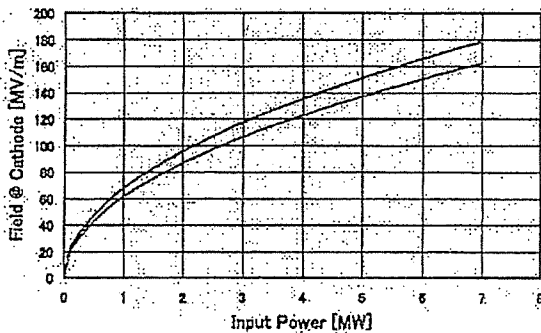
Fig. 13. Experimental setup of RF conditioning.

Fig. 14. Relation between the input RF power and the field gradient on the cathode surface.
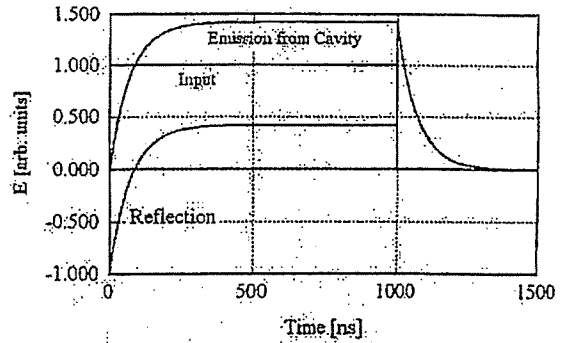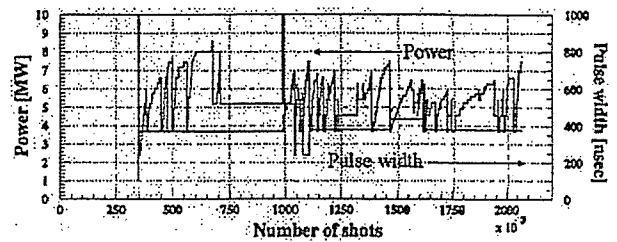

Fig. 15. RF waveform in the gun cavity.

Fig. 16. Example of RF processing of an X-band klystron. The abscissa indicates the number of shots of the klystron under 10-Hz operation.

perimental setup of the RF conditioning for the X-band klystron and waveguides is shown in Fig. 13. A low-level RF power of 300 W is fed to the klystron. This input power can be controlled by using a variable attenuator located just before the klystron input port. In order to reduce the load of the RF windows, the klystron has two output ports. The RF is damped by the dummy loads. Photo-multiplier tubes (PMT) are set to observe the light of the breakdown at the RF windows and dummy loads. The RF waveform is observed by using RF detectors at directional couplers. These signals are guided to a fast interlock system that stops the RF within 400 ns. The reflection signal from the dummy load is also used for the interlock.

The goal of the RF conditioning is to achieve 50 MW and 1 μs. However, the conditioning takes a long time. Therefore, we set a goal for an achievable level for the RF gun experiment. As Fig. 14 shows, 5 MW is required to make a field gradient of 140 MV/m at the cathode surface. Taking into account the loss around the circuit, we set a goal of 10 MW for each port (a total of 20 MW). The time structure of the electric field in the cavity is shown in Fig. 15. The target of the RF conditioning is 400 ns to fill the RF in the cavity. We have carried

out RF conditioning and have achieved a total output power of about 20 MW and a pulse width of about 400 ns under 10-Hz operation. The total operation time was about 800 hours. Fig. 16 shows an example history of RF processing.

2. High-power Experiment of the X-band Thermionic Cathode RF Gun

As mentioned above, we have achieved sufficient power and pulse width to perform an RF gun experiment. For the beam generation experiment, we constructed the beam line shown in Fig. 17. This beam line includes an X-band thermionic cathode RF gun with a solenoid coil, an alpha magnet, quadrupole magnets, and a beam diagnostics section. The alpha magnet acts as an energy selector with its inner slits. Bunch compression and beam energy estimation are also expected to occur there. To observe a beam current from the RF gun, we set current transformers (CT) at the entrance and the exit of the alpha magnet. These current transformers are also used to estimate the beam energy.

Before starting the high-power feed, we measured the return reflection from the cavity to adjust the tuning of the cavity. In order to find the lowest reflection from the cavity, we carried out frequency scanning and evaluated the return loss as a function of the frequency. The minimum return loss was observed at 11.42450 GHz (Fig.
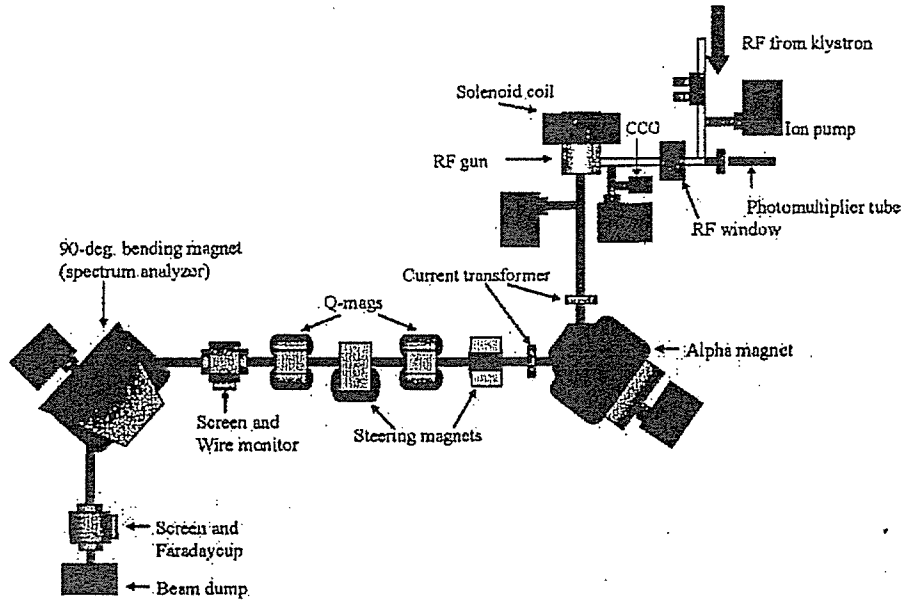
Fig. 17. Schematic view of test beam line for the X-band thermionic cathode RF gun.
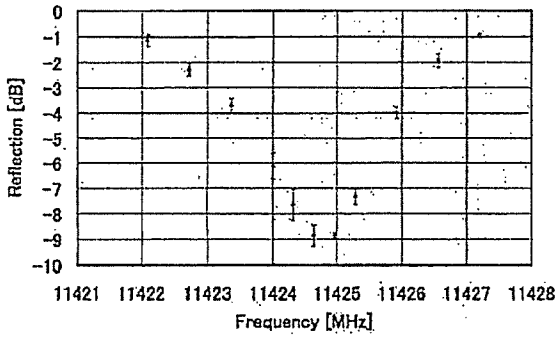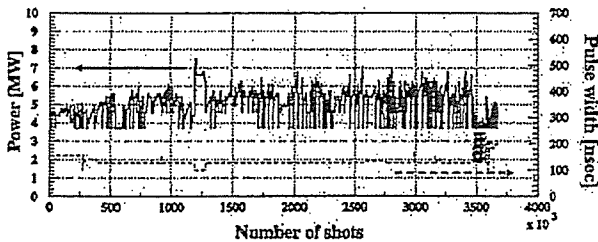

Fig. 18. Return loss at the gun cavity.

Fig. 19. Example of processing history of the X-band thermionic cathode RF gun. The abscissa indicates the number of shots of the klystron under 10-Hz operation. The solid line shows the output RF power, and the dotted line shows the pulse width of the RF.
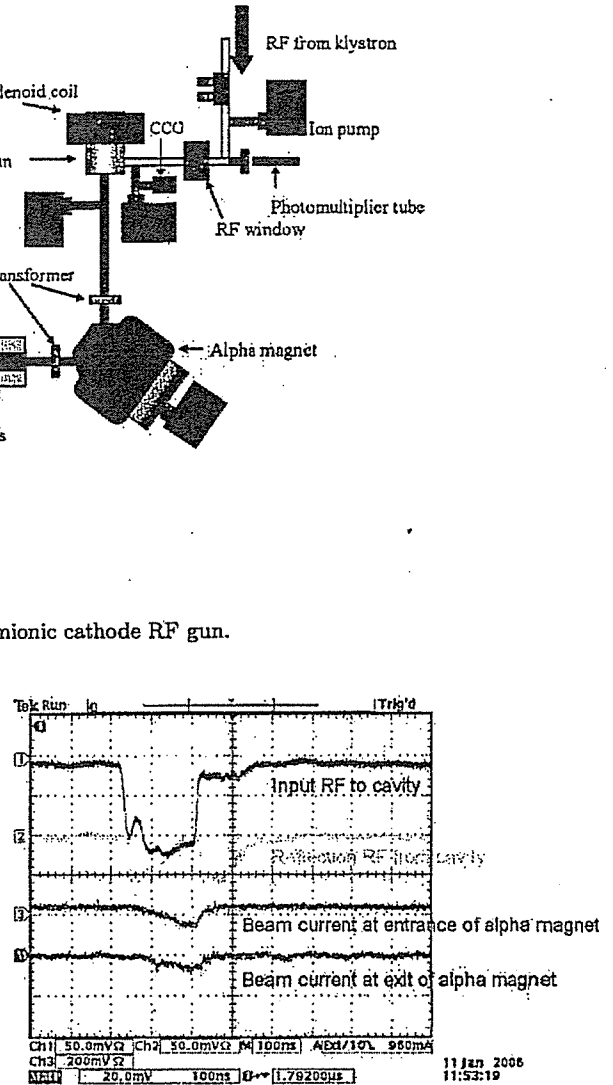

Fig. 20. RF waveform propagating forward and reflected (upper two lines) from the gun cavity. The bottom two lines show the beam currents observed at the entrance and the exit of the alpha magnet, by a current transformer.

18).

We started the RF conditioning of the RF gun cavity in April 2005. An example of the processing history is shown in Fig. 19. The total number of accumulated pulses was about 47×10^6 pulses. The maximum power and pulse width were 6 MW and 200 ns, respectively. The repetition rate was 10 Hz. Typical RF waveforms propagating forward and backward under 6 MW and 200 ns are shown in Fig. 20. The forward propagating RF has a spike. Since there are no circulators that can sustain high power at X-band frequencies, the reflected pulse returns to the klystron directly and back to the gun cavity, again affecting the forward pulse. The beam current signals observed by the current transformers are also included in Fig. 20. The beam current from the cavity is 0.15 μA. The beam energy was measured by using the alpha magnet and the current transformer. The princi-

Table 6. Experimental results of the beam generation experiment of the X-band thermionic cathode RF gun.

Beam energy	2 MeV (<10 %)
Beam current (after alpha magnet)	0.15 μA (0.01 μA)
Charge/bunch (after alpha magnet)	~1 pC/bunch (~0.1 pC/bunch)
RF input power	6 MW
RF pulse width	200 nsec

Fig. 21. Beam energy measurement by an alpha magnet.

Fig. 22. Energy spectrum of the electron beam measured by the alpha magnet (right-hand axis). The left-hand axis shows the apex of the beam trajectory in the alpha magnet.
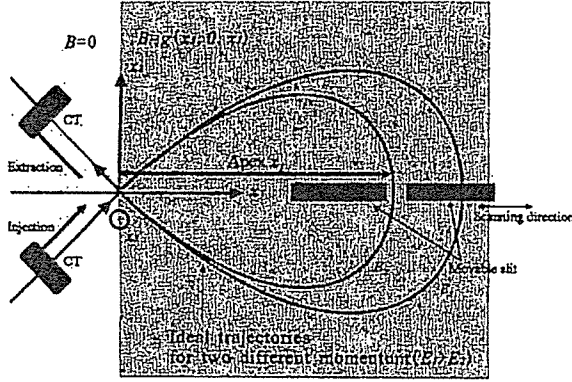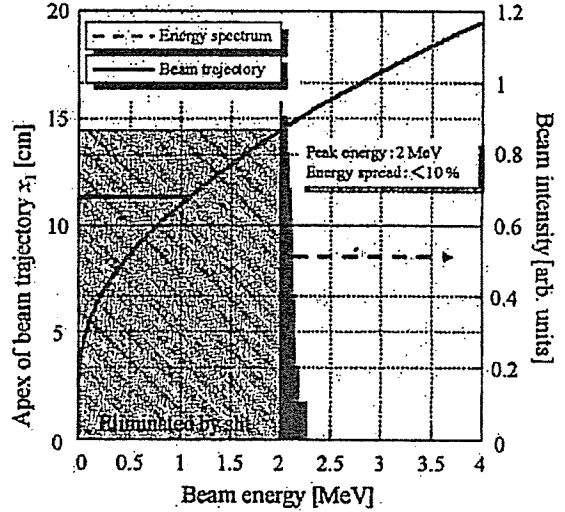
ple of the energy measurement using the alpha magnet is illustrated in Fig. 21. The ideal trajectory of a charged particle in the alpha magnet is determined by the field gradient of the alpha magnet and the kinetic energy of the charged particle. The energy spectrum is estimated by using the inner slit of the alpha magnet to observe the transmission of the beam current. Fig. 22 shows the energy spectrum of the electron beam measured by using the alpha magnet. The peak energy is 2 MeV, and the energy spread is less than 10 %. The lower-energy components are eliminated by the inside tungsten plate of the slit. The observed beam parameters are summarized in Table 6. The nominal beam current and the charge per bunch are 2 μA and 20 pC/bunch, respectively. However, the measured parameters are not consistent with the nominal values. This is due to that fact that the pulse width cannot be extended over the cavity filling time. Breakdown frequently occurred in the gun cavity. The location and the breakdown factor are being investigated. Precise diagnostics of the electron beam, such as the emittance and the bunch duration, will be carried out in the future.

V. DUAL-ENERGY X-RAY CT

The effective atomic number Z_{eff} and the electron density ρ_e of a material can be obtained by using the linear attenuation coefficients using for different energy monochromatic X-rays. The linear attenuation coeffi-

cient μ of a material can be approximately written as a function of the atomic number Z and the X-ray energy E by using a formula proposed by Jackson and Hawkes [25],

$$\mu(Z,E) \cong \rho\frac{N_A}{A}Z\left\{2\sqrt{2}Z^4\alpha^4\left(\frac{mc^2}{E}\right)\phi_0\sum_{u'}f_nu'\right.$$
$$\left.+\sigma_{KN}+\frac{Z(1-Z^{b-1})}{Z'^2}\sigma_{SC}^{coh}(Z',E')\right\}$$
$$= \rho_e(Z^4F(Z,E)+G(Z,E)), \qquad (3)$$

where ρ is the mass density, N_A is Avogadro's number, A is the atomic mass, f_nu' is a collection terms for the photoelectric absorption cross section, σ_{KN} is the Klein-Nishina cross section, and σ_{SC}^{coh} is the coherent scattering cross section of the standard element Z' at an energy of $E' = (Z'/Z)^{1/3}E$. A value of 0.5 has been proposed for the parameter b in the equation, and the standard element is taken to be oxygen [25]. If the linear attenuation coefficient is measured at two energies E_1 and E_2, the effective atomic number Z_{eff} and the electron density ρ_e can be derived by solving the following equations:

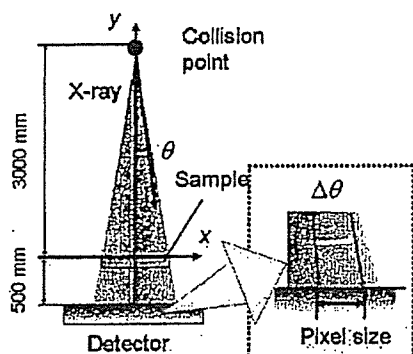$$Z^4 = \frac{\mu(E_2)G(Z,E_1)-\mu(E_1)G(Z,E_2)}{\mu(E_1)G(Z,E_2)-\mu(E_2)G(Z,E_1)},$$

Fig. 23. Schematic drawing of the dual-energy X-ray CT system.

$$\rho_e = \frac{\mu(E_1)G(Z,E_2) - \mu(E_2)G(Z,E_1)}{F(Z,E_2)G(Z,E_1) - F(Z,E_1)G(Z,E_2)}. \quad (4)$$

The effective atomic number Z_{eff} is defined for a compound or a mixture as

$$Z_{eff} = \left(\sum_i q_i Z_i^k\right)^{1/k}, \quad (5)$$

where q_i is the fractional electron content of the i-th element in the compound or mixture, and $k = 4$.

This dual-energy method is limited in that Eq. (3) cannot be applied below the K-edge energy of a material. We will operate the compact X-ray source with an electron beam energy of 35 MeV and laser wavelengths of 1064 nm and 532 nm. In this case, the maximum X-ray energies are 21.9 keV and 43.8 keV, which should allow us to identify elements up to $Z = 38$. The energy spread $\Delta E/E$ of the monochromatic X-rays generated by SR is of the order of 10^{-4}, but the energy spread in the compact X-ray source is expected to be 1 to 10 % (rms), depending on the collimator angle [5]. The energy spread of X-rays is negligible with SR light sources, but for a Compton scattering X-ray sources the energy spread affects the accuracy of the atomic number identification.

To examine the applicability of dual-energy X-ray CT with the compact X-ray source, we performed a numerical simulation for low to medium Z elements ($Z \leq 38$). We use the linear attenuation coefficients of the materials listed in the photon cross section database [26] in the simulation. The geometry of the dual-energy X-ray CT system is shown in Fig. 23. We assume a point light source and a thickness and width of the sample of 1 mm and 20 mm, respectively. In this case, X-ray photons are collimated at 3.3 mrad. We note that the X-ray energy of the Compton scattering X-ray source depends on the scattering angle. Thus, the X-ray energy is unique at each pixel of the 2D detector. When the pixel size is 0.5 mm, $\Delta\theta$ is less than 0.2 mrad, and the energy spread on a pixel is in the order of 0.1 %. This small energy spread
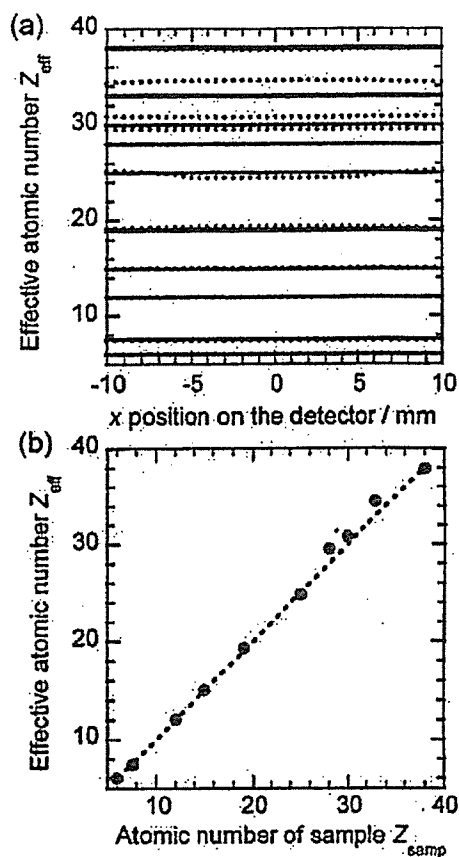

Fig. 24. Calculation results of dual-energy X-ray CT. (a) effective atomic number of each pixel for a spot size of 0.5 × 0.5 mm², and (b) average effective atomic number.

on a pixel should improve the accuracy of the dual-energy analysis. The effective atomic numbers obtained by using the linear attenuation coefficients for two energies on each pixel of the detector are shown in Fig. 24(a). The average of the effective atomic number Z_{eff} is plotted as a function of the atomic number of the sample Z_{samp} in Fig. 24(b). The accuracy of the estimated effective atomic number, $\Delta Z/Z$, is less than 3 % (rms), except for $Z = 25$ and 33. Hence, we have confirmed that the atomic number can be identified up to $Z = 38$ by using 21.9-keV and 43.8-keV X-rays with sufficient accuracy even with an energy spread of monochromatic X-rays of 1 ~ 10 %.

VI. SYNERGY OF THE DRUG DELIVERY SYSTEM AND PHYSICAL ENERGIES

The synergy of the drug delivery system (DDS) and physical energies is becoming very important, following the development of genome/protein structural anal-

ysis and molecular imaging. Physical energies are high-energy radiation (X-rays, particles), visible lasers, and microwaves (RF). These energies enable cancer therapy without surgery, adverse effects, and heavy irradiation. The development of a new dendrimer-like DDS that can react with X-rays will allow photo-dynamic therapy not only for superficial organs, but for organs deeper in a human body. Iodine delivered and attached to the DNA of cancer cells can absorb 33.2-keV X-rays and emit electrons and several characteristic X-rays. This so-called cascade radiation can kill the DNA of nearby cancer cells. Such approaches may realize a radiation-assisted DDS in the near future. Nano-magnetic particles can now be effectively delivered to diseased body parts that can be well imaged by MRI, and several improvements to the technique are under development.

Large and medium-scale simulations are extremely important for this synergy work. It is important that the flow, diffusion, pharmaceutical chemistry, radiation chemistry *etc.* for DDS be numerically analyzed.

VII. CONCLUSION

We are currently developing a compact X-ray source based on laser-electron collision. To realize a compact system, we adopt an X-band linac and a commercial Q-switched laser. The X-ray yield from an electron beam and a Q-switched Nd:YAG laser of 2.5 J/10 ns is 10^7 photons/RF-pulse (10^8 photons/sec for 10 pps). We are also designing a technique of laser circulation to increase the X-ray yield up to 10^8 photons/pulse (10^9 photons/sec). So far, we have achieved beam generation from an X-band thermionic cathode RF gun. The beam energy is 2 MeV, and the energy spread is less than 10 %. This experimental high energy ($\sim$2 MeV) beam generation from the X-band thermionic cathode RF gun is the first such achievement. However, due to breakdown in the RF gun cavity, the beam current is about 1/10 of the nominal value. We are now investigating the reasons behind the breakdown in the cavity. Precise beam-diagnostic experiments on the emittance and the bunch duration are also being planned. In addition, preparations for the beam acceleration and laser system for Compton scattering are underway. We intend to start using Compton scattering monochromatic X-rays in medical applications in 2006.

ACKNOWLEDGMENTS

REFERENCES

[1] E. Rubenstein, R. Hofstadter R, H. D. Zeman, A. C. Thompson, J. N. Oits, G. S. Brown, J. C. Giancomini, H. J. Gordon, R. S. Kernoff, D. C. Harrison and W. Thomlinson, Proc. of National Academy Sci. USA 83, 9724 (1986).

[2] S. Ohtsuka, Y. Sugishita, T. Takeda, Y. Itai, J. Tada, K. Hyodo and M. Ando, British Journal of Radiology 72, 24 (1999).

[3] M. Torikoshi, T. Tsunoo, M. Endo, K. Noda, M. Kumada, S. Yamada, F. Soga and K. Hyodo, J. Biomedical Opt. 6, 371 (2001).

[4] K. Dobashi, M. Uesaka, A. Fukasawa, H. Iijima, J. Urakawa, T. Higo, M. Akemoto and H. Hayano, Proc. of EPAC 2002, (France, 2002), p. 667.

[5] K. Dobashi, A. Fukasawa, M. Uesaka, H. Iijima, T. Imai, F. Sakamoto, F. Ebina, J. Urakawa, M. Akemoto, T. Higo and H. Hayano, Jpn. J. Appl. Phys. 44, 1999 (2005).

[6] A. Fukasawa, T. Kobayashi, M. Uesaka, J. Urakawa, T. Higo, M. Akemoto and H. Hayano, Intern. J. Appl. Electromagnetism and Mechanics 14, 221 (2001/2002).

[7] A. Fukasawa, M. Uesaka, F. Sakamoto, F. Ebina, K. Dobashi, J. Urakawa, M. Akemoto, T. Higo and H. Hayano, Nucl. Inst. Meth. B 241, 921 (2005).

[8] M. Uesaka, A. Fukasawa, K. Dobashi, H. Iijima, J. Urakawa, T. Higo, M. Akemoto and H. Hayano, Proc. of LINAC 2002, (Gyeongju, 2002), p. 626.

[9] F. Ebina, A. Fukasawa, F. Sakamoto, H. Ogino, M. Uesaka and K. Dobashi, Nucl. Inst. Meth. B 241, 905 (2005).

[10] E. Esarey, P. Sprangle, A. Ting and S. K. Ride, Nucl. Inst. Meth. A 331, 545 (1993).

[11] K. J. Kim, S. Chattopadhyay and C. V. Shank, Nucl. Inst. Meth. A 341, 351 (1994).

[12] I. V. Pogorelsky, I. Ben-Zvi, T. Hirose, S. Kashiwagi, V. Yakimenko, K. Kusche, P. Siddons, J. Skaritka, T. Kumita, A. Tsunemi, T. Omori, J. Urakawa, M. Washio, K. Yokoya, T. Okugi, Y. Liu, P. He and D. Cline, Phys. Rev. ST-AB 3, 090702/1 (2000).

[13] M. Uesaka, H. Kotaki, K. Nakajima, H. Harano, K. Kinoshita, T. Watanabe, T. Ueda, K. Yoshii, M. Kando and H. Dewa, Nucl. Inst. Meth. A 455, 90 (2000).

[14] M. Uesaka, Working Group D Summary of the Physics and Applications of High Brightness Electron Beam, (Italy, 2005).

[15] F. Carroll, Am. J. Rentgenol. 181, 1197 (2003).

[16] M.Yorozu, J. Yang, Y. Okada, T. Yanagida, F. Sakai and A. Endo, Jpn. J. Appl. Phys. 40, 4228 (2001).

[17] W. J. Brown, S. G. Anderson, C. P. J. Barty, S. M. Betts, R. Booth, J. K. Crane, R. R. Cross, D. N. Fittinghoff, D. J. Gibson, F. V. Hartemann, E. P. Hartouni, J. Kuba, G. P. Le Sage, D. R. Slaughter, A. M. Tremaine, A. J.

Wootton and P. T. Springer, Phys. Rev. ST. **7**, 060702 (2004).

[18] E. Vlieks, G. Caryotakis, D. Martin, C. A. DeStefano, W. J. Frederick J. Heritage and N. C. Luhmann, Jr., *Proc. of EPAC 2004* (Austria, 2004), p. 2837.

[19] K. Hirano, M. Fukuda, M. Takano, Y. Yamazaki, T. Muto, S. Araki, N. Terunuma, M. Kuriki, M. Akemoto, H. Hayano and J. Urakawa, Nucl. Inst. Meth. A **560-2**, 233 (2006).

[20] GLC report, KEK report 2003-7 (2003).

[21] K. Hirata, An introduction to SAD (Strategic Accelerator Design) Second Advanced ICFA Beam Dynamics

Workshop, CERN 88-04 1988.

[22] F. B. Kiewiet, O. J. Luiten, G. J. H. Brussaard, J. I. M. Botman and M. J. Van Der Wiel, *Proceedings of EPAC 2000*, (Vienna, 2000), p. 1660.

[23] J. H. Billen, *Technical Report LLA-UR-96-1834, Los Alamos National Laboratory*, 1996.

[24] L. M. Young, Los Alamos National Laboratory report LA-UR-96-1834.

[25] D. F. Jackson and D. J. Hawkes, Phys. Rep. **70**, 169 (1981).

[26] XCOM http://physics.nist/gov/XCOM.

Phase Tomography by X-ray Talbot Interferometry for Biological Imaging

Atsushi Momose*, Wataru Yashiro, Yoshihiro Takeda[1], Yoshio Suzuki[2] and Tadashi Hattori[3]

*Department of Advanced Materials Science, School of Frontier Sciences, The University of Tokyo,
5-1-5 Kashiwanoha, Kashiwa, Chiba 277-8561, Japan*
[1]*Graduate School of Pure and Applied Sciences, University of Tsukuba, 1-1-1 Tennodai, Tsukuba, Ibaraki 305-8573, Japan*
[2]*Japan Synchrotron Radiation Research Institute, 1-1-1 Kouto, Sayo, Hyogo 679-5198, Japan*
[3]*Laboratory of Advanced Science and Technology for Industry, University of Hyogo, 3-1-2 Kouto, Kamigori, Hyogo 678-1205, Japan*

The X-ray phase tomography of biological samples is reported, which is based on X-ray Talbot interferometry. Its imaging principle is described in detail, and imaging results obtained for a cancerous rabbit liver and a mouse tail with synchrotron radiation are presented. Because an amplitude grating is needed to construct an X-ray Talbot interferometer, a high-aspect-ratio grating pattern was fabricated by X-ray lithography and gold electroplating. X-ray Talbot interferometry has an advantage that it functions with polychromatic cone-beam X-rays. Finally, the compatibility with a compact X-ray source is discussed. [DOI: 10.1143/JJAP.45.5254]

KEYWORDS: phase contrast, tomography, interferometry, Talbot effect, grating, cone beam

1. Introduction

The high sensitivity achieved by X-ray phase imaging methods has been attracting increasing attention.[1,2] Because conventional X-ray imaging methods rely on absorption in an object to be inspected, weak absorbing structures, such as biological soft tissues, cannot be imaged with a sufficient signal-to-noise ratio under the allowable X-ray dosage limit. The use of X-ray phase contrast provides a way to overcome this difficulty. This is because the interaction cross section of X-ray phase shift is about a thousand times larger than that of absorption for soft tissues.[3]

Several methods have been developed for X-ray phase imaging to date, which are categorized into the interferometric method,[4–7] refraction-based method,[8–11] and propagation-based method.[12–14] Besides the methods that only generate phase contrasts, phase measurement methods are also developed, enabling quantitative image analyses, such as phase tomography.[6,7,15–19]

X-ray phase imaging is very attractive from a clinical point of view because the sensitivity to soft tissues is tremendously increased and/or X-ray dose is considerably reduced, as compared with the conventional X-ray imaging methods. Nevertheless, the introduction of these methods to medical diagnosis is very slow. This is because X-ray sources with a quality much higher than that of conventional laboratory (or hospital) X-ray sources are required in most X-ray phase imaging methods.

As for methods using a crystal interferometer[4–7] or analyzer crystal for selecting refracted X-rays,[8–11,16–19] a restriction emerges from the fact that crystal optical elements are used. The crystal optics functions under the Bragg diffraction condition; therefore, a monochromatic and parallel beam is needed with a sufficient flux. As a result, synchrotron radiation is a sole choice available for those methods with practical imaging exposure time.

The propagation-based method[12–15] relies on the detection of Fresnel diffraction, by which an outline contrast is generated at the surface and structural boundaries of a sample. The width of the outline contrast is approximately $\sqrt{\lambda\ell}$, where λ and ℓ are the X-ray wavelength and distance between the sample and detecting plane, respectively. To resolve the outline contrast, whose width is of the order of microns even when an image is detected 1 m downstream from the sample, an image detector with an effective pixel size of the order of microns or smaller is needed. Because X-rays enough to ensure a sufficient signal-to-noise ratio are needed in a pixel, a brilliant X-ray source is required consequently. Many experiments are therefore performed at synchrotron facilities. The contribution of the outline contrast can be observed using a detector of a pixel size larger than the above estimation, and a medical apparatus has been developed on the basis of this usage for use in hospitals.[20] However, for quantitative phase measurement and thereby phase tomography, Fresnel diffraction must be observed with a sufficient spatial resolution and a sufficient signal-to-noise ratio, which are attained by synchrotron radiation.[15]

Recently, X-ray differential interferometry that employs transmission gratings has been studied for X-ray phase imaging,[21–25] which is potentially compatible with compact X-ray sources. X-ray Talbot interferometry (XTI)[22] shown in Fig. 1 is an X-ray differential interferometer consisting of a phase grating (G1) and an amplitude grating (G2). XTI may provide an opportunity for the instrumentation outside synchrotron facilities, because it functions in principle with a cone beam with a broad energy band width.

The principle of XTI is the same as that of optical Talbot interferometry,[26,27] but the fabrication of an amplitude
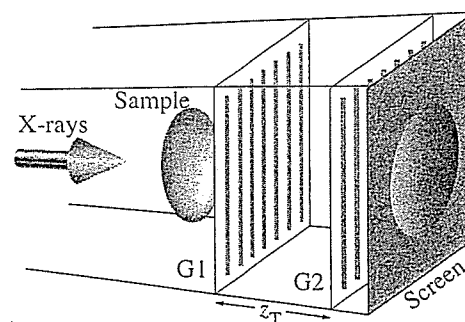

Fig. 1. Configuration of XTI, where two transmission gratings (G1 and G2) are arranged in line along X-ray axis.

*E-mail address: momose@exp.t.u-tokyo.ac.jp

X-ray grating is a difficulty that needs to be overcome to realize XTI. Because of the high penetrating power of X-rays, a thick pattern must be fabricated to block X-rays fully. At the same time, the period of the grating should be of the order of microns, as explained later according to the principle of XTI. The fabrication of a pattern with such a high aspect ratio is not straightforward.

A capillary plate, which has a two-dimensional array of holes in a lead glass plate with an aspect ratio that meets already the requirement for XTI, is a candidate device for the amplitude X-ray grating.[28] However, its quality, such as the uniformity of the pitch of the hole array, is currently unsatisfactory. A line and space (L&S) pattern is used for a simple and typical grating and available for XTI. However, the fabrication of a high-aspect-ratio L&S pattern is difficult using conventional lithographic techniques. However, X-ray lithography is attractive for that purpose, and in this study we used a grating fabricated by X-ray lithography and electroplating of gold,[29] which was selected as a material for blocking X-rays because of its high absorption coefficient and technical convenience in the fabrication process.

In this paper, theoretical aspects of XTI are described first, including the procedure of phase tomography. Then, we report evaluation results of an X-ray Talbot interferometer constructed with gold gratings. We performed phase tomography measurements on biological soft tissues with the interferometer using synchrotron radiation, and reconstructed images are presented next. Finally, future prospects of XTI are discussed.

2. X-ray Talbot Interferometry

2.1 Principle of phase imaging

The principle of XTI was described in a previous paper[22] but again described here, adding more details, for the following explanation of phase tomography based on XTI.

The function of XTI is based on the X-ray (fractional) Talbot effect[30] discovered originally in the visible light region,[31] which is known as a self-imaging effect by an object with a periodic structure under coherent illumination. While a transmission image becomes blurry with increasing distance from an object to an imaging plane under normal illumination, self-images are reconstructed at specific distances from a periodic object to an imaging plane by the Talbot effect. This phenomenon is understood as a result of Fresnel or Fraunhofer diffraction.

Let us consider a situation in which a grating of a period d is illuminated coherently with unit-amplitude plane-wave X-rays of wavelength λ. Given the complex transmission function $T(x, y)$ of the grating with a Fourier expansion series

$$T(x, y) = \sum_n \alpha_n \exp\left(2\pi i \frac{nx}{d}\right), \quad (1)$$

the wave field $E(x, y, z)$ behind the grating is written as

$$E(x, y, z) = \sum_n \beta_n(z) \exp\left(2\pi i \frac{nx}{d}\right) \quad (2)$$

under a paraxial approximation, where

$$\beta_n(z) \equiv \alpha_n \exp(-\pi i \lambda z n^2 / d^2). \quad (3)$$

Here, the optical axis is parallel to the z axis, and the grating

is on the (x, y) plane ($z = 0$) and has periodicity in the x direction. Equations (2) and (3) imply that the periodic pattern in the wave field varies and oscillates as induced by propagation. The intensity of the wave field is given by

$$I_s(x, y, z) = |E(x, y, z)|^2 = \sum_n a_n(z) \exp\left(2\pi i \frac{nx}{d}\right), \quad (4)$$

where

$$a_n(z) \equiv \sum_{n'} \beta_{n+n'} \beta_{n'}^*. \quad (5)$$

The distances z_T given by

$$z_T = md^2 / \lambda, \quad (6)$$

where m is an integer for an amplitude grating or a half integer for a phase grating, are particularly interesting. If m is an even integer, $\beta_n(z_T) = \alpha_n$; therefore, a wave field whose complex amplitude is the same as the complex transmission function of the grating is generated (Talbot effect). If m is an odd integer, $\beta_n(z_T) = -\alpha_n$, and a wave field with a complex amplitude of $T(x + d/2)$ is generated (a case of fractional Talbot effect); that is, the contrast is inverted. When a phase grating is used, no intensity patterns are observed at the distances. However, if m is a half integer, the phase modulation pattern $T(x) = \exp[i\phi(x)]$ is converted into intensity patterns, which are also called self-images in this work, as given by

$$|E(x, y, z_T)|^2 = 1 \pm \sin\{\phi(x) - \phi(x + d/2)\}, \quad (7)$$

where $\pm$ corresponds to cases in which $m - 1/2$ is even and odd.[32] Visibility is therefore at the maximum when the magnitude of phase modulation is $\pi/2$ while a π phase grating is used in many applications because $\pm$1st-order diffractions are enhanced, suppressing the 0th order. The self-image of a $\pi/2$ phase grating is understood as a constructive superposition of interference fringes mainly between neighboring orders (i.e., 0th and $\pm$1st orders, $\pm$1st and $\pm$2nd orders, ...).

Under partial coherent illumination, the visibility of a self-image is degraded and its influence can be reflected in eq. (4) by replacing $a_n(z)$ with $\mu(n\lambda z/d)a_n(z)$, where μ is the complex degree of coherence, which is given by the Fourier transform of the distribution of an X-ray source, according to the van Cittert–Zernike theorem.[33]

Next, let us consider a case in which the incident X-ray wave is deformed due to the phase shift $\Phi(x, y)$ caused by an object placed in front of the grating. In this case, the self-image is also deformed as illustrated in Fig. 2 and its intensity is given by

$$I_s(x, y, z) = \sum_n a_n'(x, y, z) \exp\left[2\pi i \frac{n}{d}(x - z\varphi_x(x, y))\right], \quad (8)$$

where

$$\varphi_x(x, y) = \frac{\lambda}{2\pi} \frac{\partial \Phi(x, y)}{\partial x} \quad (9)$$

and $a_n(z)$ has been replaced with $a_n'(x, y, z)$, which takes into consideration the effect of X-ray attenuation by the sample. The amount of deformation is proportional to z.

It is therefore possible to detect the object by analyzing the deformed self-image by using an image detector with
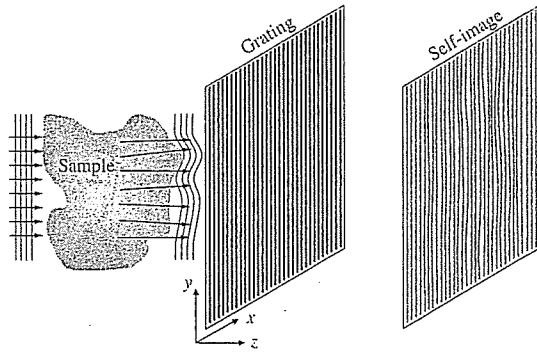
Fig. 2. Deformation of self-image by refraction at sample placed in front of grating.

a spatial resolution below d (of the order of microns). However, an X-ray image detector with such a resolution is rare. Instead XTI uses another grating at the position of the self-image, as illustrated in Fig. 1. If the period of the second grating is almost the same as that of the self-image, a moiré fringe pattern is generated by the superposition of the deformed self-image and the pattern of the second grating. The deformation of the self-image is also reflected on the moiré pattern. Because a typical fringe spacing is much larger than d, normal X-ray image detectors are available.

Giving the transmission function $t(x, y)$ of the second grating with a Fourier expansion series as

$$t(x, y) = \sum_n b_n \exp\left(2\pi i \frac{nx}{d}\right), \qquad (10)$$

a moiré pattern is given by

$$I(x, y, z) = I_s(x, y, z) \times t(x, y)$$
$$= \sum_n a'_n(x, y, z) b_{\bar{n}} \exp\left\{2\pi i \frac{n}{d}\left(y\theta + z\varphi_x(x, y) + \chi\right)\right\}, \qquad (11)$$

where θ ($\ll 1$) and χ are the relative inclination and displacement, respectively, in the (x, y) plane of the second grating against the first. The factor describing the contrast with the period of d has been averaged out.

2.2 Phase tomography

The X-ray phase shift $\Phi(x, y)$ is written as

$$\Phi(x, y) = \frac{2\pi}{\lambda} \int \delta(x, y, z) \, dz, \qquad (12)$$

where $\delta(x, y, z)$ is the refractive index decrement from unity. Therefore, if phase shifts are measured in plural projection directions, $\delta(x, y, z)$ is reconstructed with the algorithm of computed tomography. This is X-ray phase tomography.[6] The quantitative measurement of $\Phi(x, y)$ is therefore significant. In the case of XTI, φ_x is determined from moiré patterns. Then, Φ is obtained by integration, enabling X-ray phase tomography.

To determine φ_x from the moiré patterns, phase-shifting interferometry (or fringe-scanning method)[34] is available. Normal phase-shifting interferometry assumes a two-beam interference, which generates a sinusoidal fringe profile in general given by $A + B \cos \Phi$, where A and B are the average intensity and fringe contrast. By introducing a phase difference that varies with a step of $2\pi/M$ (M: integer), interference patterns

$$I^{(k)}(x, y) = A(x, y) + B(x, y) \cos\left\{\Phi(x, y) + \frac{2\pi k}{M}\right\} \qquad (13)$$
$$(k = 1, 2, \ldots, M)$$

are measured, and Φ is calculated using

$$\Phi(x, y) = \arg\left[\sum_{k=1}^{M} I^{(k)}(x, y) \exp\left(-2\pi i \frac{k}{M}\right)\right]. \qquad (14)$$

In the case of XTI that causes multibeam differential interference, by changing χ in eq. (11) with a step of d/M (M: integer), moiré patterns

$$I^{(k)}(x, y, z_T) = \sum_n a'_n(x, y, z_T) b_{\bar{n}}$$
$$\times \exp\left\{2\pi i \frac{n}{d}\left(y\theta + z_T \varphi_x(x, y) + \frac{kd}{M}\right)\right\} \qquad (15)$$

are measured. If the 0th and ±1st orders are dominant, it is clear that the operation of eq. (14) is available; that is,

$$\frac{2\pi}{d}(y\theta + z_T \varphi_x(x, y))$$
$$= \arg\left[\sum_{k=1}^{M} I^{(k)}(x, y, z_T) \exp\left(-2\pi i \frac{k}{M}\right)\right]. \qquad (16)$$

The influence of higher orders is considered as below. The substitution of eq. (15) into the right hand side of eq. (16) yields

$$\arg\left[\sum_n a'_n(x, y, z_T) b_{\bar{n}} C_{n,M} \right.$$
$$\left. \times \exp\left\{i2\pi \frac{n}{d}(y\theta + z_T \varphi_x(x, y))\right\}\right], \qquad (17)$$

where

$$C_{n,M} \equiv \sum_{k=1}^{M} \exp\left\{2\pi i \frac{k}{M}(n-1)\right\}$$
$$= \begin{cases} M & \text{if } n - 1 = qM \\ 0 & \text{otherwise} \end{cases} \quad q: \text{integer}. \qquad (18)$$

The combinations of n and M that yield non-zero values of $C_{n,M}$ are shown in Table I, which suggests that if a sufficiently large number is selected for M, the influence of higher orders is cancelled out and eq. (16) is available.[35]

Here, it should be noted that even orders can be ignored if the gratings have 1:1 L&S patterns. Then, when $M = 5$, the lowest order is ninth, which causes an error in calculating φ_x using eq. (16). The magnitude of such a high order is very small normally. In addition, actual grating patterns are not

Table I. Combinations of n and M indicated by "e" yield non-zero values of $C_{n,M}$ and cause errors in calculating φ_x using eq. (16).

M	Harmonics ($|n|$)							
	2	3	4	5	6	7	8	9
3	e	—	e	e	—	e	e	—
4	—	e	—	e	—	e	—	e
5	—	—	e	—	e	—	—	e
6	—	—	—	e	—	e	—	—
7	—	—	—	—	e	—	e	—
8	—	—	—	—	—	e	—	e

completely rectangular and the spatial coherency of X-rays that impinge on the gratings is normally incomplete. These factors decrease higher orders and contribute to reducing errors in calculating φ_x using eq. (16). Thus, $M = 5$ is a kind of magic number suitable for applying the technique of phase-shifting interferometry to XTI. The absorption contrast caused by the sample, which is involved in a'_n, is eliminated by this procedure, and the resultant image maps purely the differential phase shift φ_x.

Normally, φ_x is determined by measurements with and without a sample. Then, the effect of θ on eq. (16) is removed by subtraction. In addition, the effect of the imperfection of gratings and/or deformed wavefronts of incident X-rays are excluded as well.

The right term of eq. (16) involves the operation of arctangent, whose value ranges from $-\pi$ to π. Therefore, when X-rays are refracted partially exceeding the amount corresponding to the range, jumps between $-\pi$ and π are found in the resultant image obtained by the calculation of eq. (16). In such a case, we need a process for *unwrapping* the jumps by adding (subtracting) 2π to (from) one of the pixels neighboring across the jumps. When the jump lines are clear, the procedure is completed without errors. However, the jump lines become unclear occasionally when the data is noisy or when regions of steep value changes are contained. Sophisticated techniques are developed to enable unwrapping in such cases, and we used a cut-line algorithm[36] in the present study.

Finally, Φ is obtained by calculating

$$\Phi(x, y) = \frac{2\pi}{\lambda} \int \varphi_x(x, y)\, dx + C, \qquad (19)$$

and the constant of integration C is determined by the fact that a sample is surrounded by a null region in the measurement by tomography; that is, $C = 0$. By repeating this measurement at various angular positions of the sample rotation, one can reconstruct $\delta(x, y, z)$ using a conventional algorithm in computed tomography.

One can skip this integration process if an algorithm with a filter function for beam-deflection optical tomography[37] is used; in the case of the convolution-backprojection method,

$$H(h\Delta x) = \begin{cases} \dfrac{1}{\pi^2 h \Delta x} & h:\ \text{odd} \\ 0 & h:\ \text{even} \end{cases} \qquad (20)$$

is the filter function to be used, where Δx is the pixel size.

As a summary of this section, images at each image processing step described above are shown in Fig. 3 using the data of the phantom experiment reported previously.[23]

3. Experiments

3.1 Grating

We selected gold as a material for the grating pattern because its absorption coefficient is comparatively large. Nevertheless, the thickness should be much more than ten microns. As for the grating period, it should be smaller than or comparable to the X-ray spatial coherence length, which is several microns typically, and as a result a pattern of a high aspect ratio must be fabricated.

Although microfabrication by optical lithography is routinely performed, it is difficult to form a L&S pattern
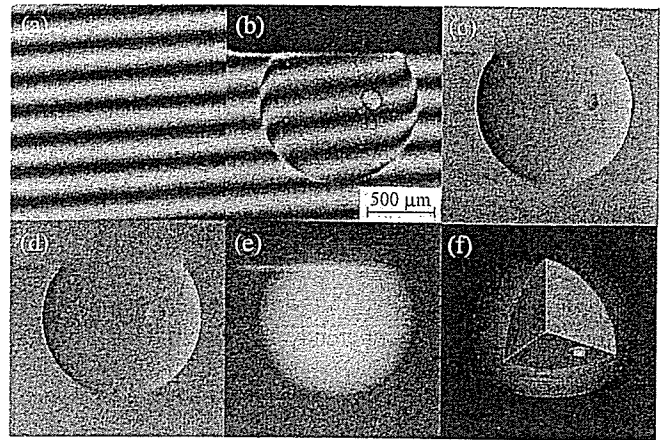

Fig. 3. Images at each step of phase tomography with XTI. A moiré pattern (a), which was due to the relative inclination (θ) of the grating against the other, is deformed by the differential phase shift caused by a sample (plastic sphere about 1 mm in diameter with some air bubbles in it) placed in the field of view, as shown in (b). (c) was obtained by a five-step fringe scan. The effect of θ was removed using (a). Because (c) is the output of eq. (16), the image is *wrapped*, and after an unwrapping procedure, (d) that exhibits φ_x is obtained. Black-white jumps observed in the outline region of the sphere in (c) are compensated. (e), which is to be input to the reconstruction algorithm of tomography, is obtained through the spatial integration of (d). Repeating this series of procedure at every angular position of the sample rotation, a three-dimensional image (f) mapping the refractive index is reconstructed, where one quadrant has been cropped to show the inside.

whose thickness exceeds ten microns. A solution is found in the field of X-ray lithography, which enables the formation of a high-aspect-ratio structure, taking advantage of the property of X-rays, that is, they tend to go straight in comparison with light of longer wavelengths. In this study, we used an X-ray amplitude grating fabricated by X-ray lithography and gold electroplating, as described below.

The synchrotron radiation beamline 11 of NewSUBARU, Japan, which is dedicated to Lithographie Galvanoformung Abformung (LIGA) fabrication, was used. A 30 μm X-ray resist film (MAX001, Nagase ChemteX) was spin-coated on a 200-μm Si wafer with a 0.25-μm Ti layer, and then a 4-μm L&S resist pattern ($d = 8$ μm) was fabricated by X-ray exposure. Gold lines were formed by electroplating between resist lines, which were left after the electroplating to support the gold lines (Fig. 4). The effect of absorption by the X-ray resist is negligible. The height of the gold lines
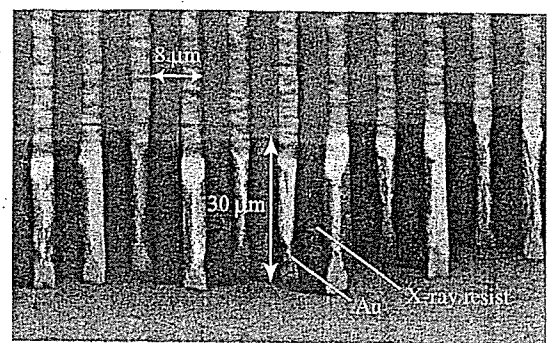

Fig. 4. SEM image of X-ray amplitude grating fabricated by X-ray lithography and gold electroplating. This grating was used for the second grating in XTI.

was nearly 30 μm, and the effective area of the grating was $20 \times 20\,\text{mm}^2$.[29]

The first grating was also fabricated in a similar manner, except that UV lithography was used, and had a gold pattern, which was much thinner than that of the second. The thickness was experimentally evaluated to be optimal for X-rays of about 0.065 nm for a $\pi/2$ phase grating. An amplitude grating is available for the first grating, but a phase grating is superior to an amplitude grating in that X-ray intensity is twice at an image detector and that the requirement for spatial coherency is moderated because z_T is reduced by one-half.

3.2 Performance of XTI

An X-ray Talbot interferometer was arranged at the beamline 20XU of SPring-8, Japan, where undulator X-rays were available at 245 m from the source point. The vertical source size of synchrotron radiation is normally much smaller than the horizontal size. However, because the effect of the instability of the beamline monochromator existed, the gratings were aligned so that the gold pattern was almost vertical. Then, spatial coherency was determined by horizontal source size. Strictly, in the present case, source size was determined by the front-end slit 400 μm in width located 214 m upstream from the grating. The spatial coherence was certainly larger than d (= 8 μm).

Figure 5 shows moiré patterns observed with 0.065-nm X-rays with the visibility as a function of the distance between the gratings. Here, θ was 1.3° and therefore the moiré fringes were generated. Although this study was performed assuming that synchrotron radiation is a plane wave, strictly a spherical wave with a small curvature was introduced into the interferometer, and its effect was observed as the inclination of fringes; that is, the horizontal component of spatial frequency is due to the mismatch of the period between the second grating and the self-image of the first grating, which was enlarged by slightly spherical-wave illumination.

At $z = d^2/2\lambda$, which was the best position for XTI with a $\pi/2$ phase grating, the fringe visibility exceeded 0.8. With increasing the distance, visibility minimized at $z \approx d^2/\lambda$ and again increased, indicating that this phenomenon was induced by the fractional Talbot effect. Strictly, a minimum was found at a distance slightly shorter than d^2/λ. This is considered to be due to the coexisting amplitude modulation caused by the first grating.

The influence of higher orders when using eq. (16) was commented above. Figure 6 shows the Fourier-transforms of the moiré patterns shown in Fig. 5. In Fig. 6(b), that is, the
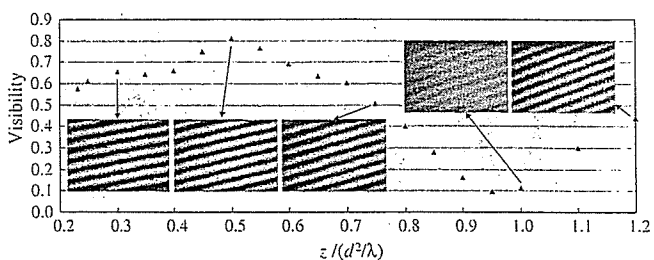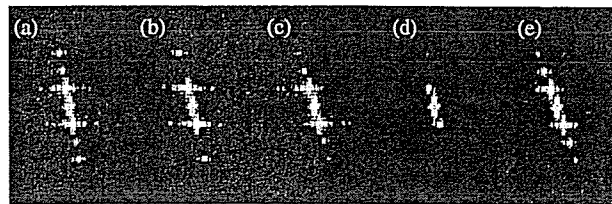

Fig. 6. Fourier-transforms of moiré patterns shown in Fig. 5 in the same order.
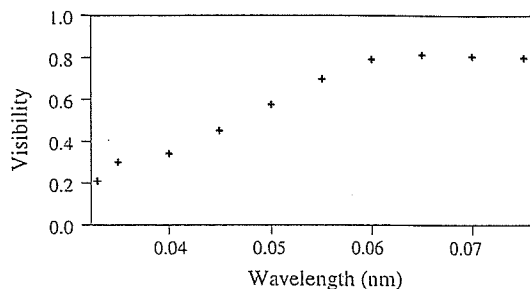

Fig. 7. Visibility of moiré pattern as function of X-ray wavelength. The distance between gratings was kept at $d^2/2\lambda$.

Fourier transform of the moiré pattern of the best visibility, spots of 0th, 1st, and 3rd orders existed, and those of higher orders and even orders were not detected. This result confirmed that the selection of 5 for M as discussed above was reasonable for the experiments of phase tomography that will be presented below. However, at the same time, it was found that other Fourier-transforms exhibited even orders as shown in Fig. 6. Therefore, one should be careful when XTI is operated with the grating separation widely different from $d^2/2\lambda$ even if the visibility is still high.

Next, keeping the condition $z = d^2/2\lambda$, the visibility was plotted as a function of λ (Fig. 7). This result shows that the Talbot interferometer functioned in a wide energy range; the visibility was over 0.3 even at 0.04 nm (31 keV). The availability of the interferometer at higher energy is meaningful because the observation of high-density tissues such as bone and calcification becomes more feasible, revealing soft tissue structures in the same view.

3.3 Phase tomography of biological samples

The X-ray Talbot interferometer was used for the tomographic observation of biological soft tissues. A sample was fixed on the tip of a rotation rod and immersed in formalin filling a cell. Because of the problem of bubble generation in the cell due to intense X-ray irradiation, beam intensity was moderately reduced by undulator-gap detuning. The flux density at a sample was approximately 10^{11} photons $\text{mm}^{-2}\,\text{s}^{-1}$.

The measurement of $\varphi_x(x, y)$ by a five-step fringe scan was repeated at each angular position of the sample rotation with a step of 0.72° over 180°. Images were recorded using a CCD camera coupled with optical lens and a phosphor screen, whose effective pixel size was 4.34 μm. The tomograms presented below are therefore formed by voxels 4.34 μm on one side. Exposure times for recording a moiré pattern were 1.0, 0.2, and 0.25 s for Figs. 8, 9, and 10, respectively.

Fig. 5. Moiré patterns and their visibilities observed by XTI at various spacings between two gratings. $\lambda = 0.065\,\text{nm}$.